Development of a Laboratory Oscillating Surge Wave Energy Converter

Ama R. Hartman

A thesis

submitted in partial fulfillment of the

requirements for the degree of

Master of Science in Mechanical Engineering

University of Washington

2022

Committee:

Brian L. Polagye

Michelle H. DiBenedetto

Tim Mundon

Program Authorized to Offer Degree:

Mechanical Engineering

University of Washington

Abstract

Development of a Laboratory Oscillating Surge Wave Energy Converter

Ama R. Hartman

Chair of the Supervisory Committee:
Brian L. Polagye
Department of Mechanical Engineering

Ocean wave energy conversion is a promising solution to growing energy demands across the globe, particularly for island and coastal communities. Oscillating Surge Wave Energy Converters (OSWECs) harness energy through a buoyant flap, typically bottom-hinged, which oscillates in response to surging wave forces. With OSWEC design still an active area of research, the technology is not yet mature enough for grid-scale or "Blue Economy" applications. There are numerous experimental studies of OSWECs to-date, with topics ranging from general performance to array behavior. However, further experimental research remains essential to address knowledge gaps in device hydrodynamics and control. While many laboratory-scale experimental OSWECs have been developed, these have been sparsely instrumented and rarely used to understand or optimize control strategies.
This thesis focuses on developing the driveline for a laboratory-scale experimental OSWEC intended to study hydrodynamics and control. The device is unique, relative to prior

experimental work, given it is designed to emulate power-take-off using a servo-motor and gearbox protected by a submersible housing directly underneath the flap, reducing losses and potential hydrodynamic interactions from a chain drive or hydraulic system. However, the gearbox and rigid shaft coupling included in the driveline may introduce differences in commanded and realized flap position due to backlash or torsion. Characterizing this behavior is a necessary step in readying the driveline for experimental work. Additionally, future experiments may require accurate control of device position or driveline torque, so experimental characterization of motor torque and velocity constants is another step required prior to OSWEC experimentation.

To study positional differences between the motor and external shaft as a result of backlash and coupling torsion, a benchtop dynamometer was designed and built. The benchtop fixture secures the following components in-line: a servomotor, gearbox, rigid shaft coupling, encoder, six-axis load cell, bearing, flexible shaft coupling, and a magnetic particle brake. During experiments, the motor commands a sinusoidal velocity profile similar to that seen by the OSWEC during regular operation, and the particle brake commands a resistive torque proportional to the shaft rotational velocity. Position measurements are captured by an encoder internal to the motor as well as an encoder on the shaft outboard of the gearbox and coupling. In order to characterize torsional deflection of the shaft relative to the motor, position of the motor and shaft are compared alongside driveline torque measurements captured by the load cell. Shaft oscillations are found to have a smaller amplitude and are shifted in phase in comparison to motor oscillations.

Amplitude attenuation is found to be linearly correlated with root-mean-squared driveline torque, and phase shift linearly correlated with root-mean-squared motor velocity. These relationships are used to create a position control correction which reduces positional differences between the motor and shaft by a factor of two.

Derivatives of the benchtop dynamometer are used to experimentally determine motor torque and voltage constants. Hardware setup remains unchanged for the study of motor torque constant during which torque control is employed for the motor while the particle brake is commanded to resist with maximum torque to maintain a stationary driveline. The torque constant is calculated using a linear fit between driveline torque, as measured by the load cell, and command current, as delivered to the motor, and is found to be in agreement with motor specifications. However, significant variability in the calculated torque constant between experiments suggests that precise torque control will require real-time corrections (i.e., closed loop control on measured mechanical torque). During velocity constant testing, the particle brake is disengaged from the dynamometer driveline and the motor is operated under velocity control. The velocity constant is then calculated using a linear fit between the driveline velocity and motor command voltage. The spread of velocity constant values is only 2.8% of the mean, suggesting accurate velocity control could be achieved with minimal real-time corrections.

TABLE OF CONTENTS

LIST OF FIGURES

LIST OF TABLES

ACKNOWLEDGMENTS

Thank you to Professor Brian Polagye for the mentorship, support, and steady confidence.

Additional thanks to Corey Crisp for the design, assembly, and help troubleshooting benchtop rig electronics, Erik Skeel for the design and assembly of motor mounting hardware, Cassie Riel for the design of encoder and load cell support components, Brittany Lydon for the help estimating ideal PTO damping coefficients, Dr. Curtis Rusch for development of the moving window differentiator, and to members and alumni of the Marine Renewable Energy Laboratory for the guidance and friendship.

Finally, thank you to my mom for instilling in me the meaning of hard work and a drive for improvement, and to my family for the inspiration, love, and continual support.

Funding for this work was provided by the United States Naval Facilities Engineering Command, the United States Department of Energy, and the Alice C. Tyler Trust.

DEDICATION

To my family.

Chapter 1

INTRODUCTION

1.1 Background

Developing further sources of renewable energy is a known global necessity [1], [2]. Ocean waves are a promising renewable resource due to their high energy density and low resource intermittency in comparison to other renewable resources, such as wind and solar. But this energy density and its extreme values during storms makes the design of Wave Energy Converters (WECs) challenging. Oscillating Surge Wave Energy Converters (OSWECs) are one WEC archetype which aim to harness ocean energy through a buoyant, hinged flap which oscillates primarily in response to surge forces. OSWECs are particularly promising nearshore where water surge motion is increased due to shoaling [3] and the hingepoint can be fixed to the seafloor, reducing complexity associated with floating systems. Like all WECs, the hydrodynamics of OSWEC operation are not fully understood, limiting their integration into coastal energy grids or smaller-scale Blue Economy applications.

OSWEC performance was first seriously studied as part of the development of Oyster, an 18 m wide [4], 315 kW WEC developed by Aquamarine Power in the UK from the early 2000's to about 2010, when the company declared bankruptcy [5]. Chronologically, academic studies of Oyster begin when Whittaker et al. used 1:40 scale testing to show that both tidal variations and increasing angle of incidence of an incoming wave will cause reductions in

power capture, with the reduction proportional to the cosine of said angle in the case of an oblique wavefront [6]. This work was later confirmed by Henry in 2009 when he also found that surface piercing flaps perform significantly better, as wave overtopping greatly reduces power capture [4]. Some of the only experimental studies on OSWEC control are from this period of Oyster scale testing when Henry found that optimum damping for a given OSWEC and sea state can be determined from a parabolic relationship between power and root-mean-square (rms) torque, and that a biased PTO scheme which applies increased resistance as the flap moves in the direction of wave travel can increase power capture [4].

Since this early work, numerous studies have been conducted with a focus on hydrodynamic analysis. In 2015, Wei et al. [7] set out to study the influence of viscosity on the flap using a high-speed camera and a flap outfitted with pressure sensors. They found local vortex shedding during each half-wave period, and determined that flap hydrodynamics are dominated by diffraction and radiation, with viscous drag playing a negligible role as scale and flap width increase. Later work on OSWEC hydrodynamics studied trends of capture width ratio (CWR), a measure of hydrodynamic efficiency defined as the ratio of mechanical power harnessed to wave power per unit crest length. Ning et al. found that CWR decreases with increasing wave magnitude [8], but Brito et al. found insignificant differences in CWR from waves with differing amplitudes [9]. This discrepancy could be attributed to differences in experimental approach, as the flap used by Ning et al. simulated PTO with a magnetic particle brake and experiments were run in an open basin, while the flap used by Brito et al. had a hydraulic PTO and experiments were two-dimensional (performed in a narrow channel).

Additional hydrodynamic study has been on the topic of device loading, with early work focusing on standard operational loads. In 2009, Henry found that peak heave and surge resultant loads act around -16°from the horizontal plane, and maximum loads are not significantly dependent on the power take-off configuration (e.g., similar loads for free-oscillation or a damped PTO). Later studies on hydrodynamic loading are concentrated on slamming, an event in which a large wave overtops the flap and prevents oscillation until the wave crest surpasses, thus allowing the flap to accelerate into the incoming trough where it slams into the next wavefront. Slamming events are characterized by high device loads and rotary travel. Henry found that the highest slam pressures occur in the horizontal center of the flap [10], [11], with an impulsive load starting low before backing off gradually as it travels upwards during the event [10], [12], [13], [14]. Lamont-Kane later found differences in slam pressures between two-dimensional experiments carried out in a narrow channel and three-dimensional experiments carried out in a sufficiently wide basin [14].

The role of flap design has also received significant attention. Early work on the ideal flap shape by Henry [4] showed that increased thickness, rounded edges, and edge-affectors (components added to selectively increase flap edge thickness) can reduce viscous losses, with the edge-affectors also increasing optimal PTO damping torque. Additionally, positioning a large diameter, air filled tube at the top of the flap can improve performance by increasing spring stiffness at the peaks of oscillation, as well as by preventing losses caused by overtopping. Henry also found that ideal flap density depends on the period of incoming waves, with higher density preferred for waves with longer periods. However, the ideal flap may not have uniform density. For example, Ning et al. [8] found that a lowered center of gravity improves

performance. Variable flap geometry to reduce loads have also been explored. For example, Choiniere et al. [15], [16] considered an OSWEC with horizontal baffles which could be fixed open or closed. Fixing the baffles open was found to reduce the pitching excitation moment by up to more than half of the moment experienced by the closed baffles, the configuration synonymous with a solid flap, which could be useful during extreme storm events. Natural frequency of the flap with open baffles was also significantly higher in comparison with the closed configuration, which is consistent with reduced hydrodynamic resistance [16].

In general, some work has been done to develop numerical models to describe OSWEC behavior, but in many cases the models are unable to accurately describe the system hydrodynamics when compared to experimental data. This is evident in studies of added mass, vortex behavior, overtopping, and loading during large amplitude oscillations [17], [18], [19], [20]. Added mass is a particularly important component to model accurately, as Henry found that it is a dominant contributor to flap inertia [4] (i.e., added mass dominates over flap static inertia). In addition to exploring areas of OSWEC hydrodynamics where current numerical models are inaccurate, experimental data provides a foundation for validation of new models.

To accommodate the wide breadth of experimental OSWEC research topics to-date, there have been a number of experimental devices developed. All devices are scaled, with widths ranging from 0.14 [21] to 1.31 m [17], and the majority of them are just under a meter wide. Capabilities of existing devices are limited to the scope of experiments they have been designed for. For example, flaps designed into arrays [21], [22] are unable to be used to investigate individual flap behavior, as interactions with nearby flap hardware is unavoidable.

Some flaps have been designed with no PTO to run free-oscillation experiments [12], [13], [15]. This is useful for investigations on slamming, but falls short of the hardware required to study control or loading during standard operation. Other OSWECs use hydraulic piston PTOs which have been found to introduce nonlinear WEC response, and can limit the response time for control strategy testing [4], [9]. Similarly, many make use of brakes to emulate PTOs, which only allow for reactionary control schemes and may be subject to nonlinear braking responses [6], [8], [10], [20], [23]. A small number use a servo motor to simulate PTO, but the use of a timing belt and gearbox can introduce unwanted control lag [22], [24]. All of these approaches were suitable for the specific use-cases studied and have led to important findings. They also help to pave the way for the design of new experimental OSWECs.

1.2 OSWEC System Design

We worked in collaboration with design engineers at the Applied Physics Laboratory to develop a laboratory-scale OSWEC (Fig. 1.1) with the goal of a research test bed that could explore knowledge gaps in OSWEC hydrodynamics, geometry, and control. The flap is designed to be modular in shape and instrumentation. The core flap has two edge profiles that can easily be swapped out, and the face has 15 pressure sensor mount locations with dummy sensors installed in their absence as necessary to retain inertial properties throughout experiments. The internal flap structure consists of 80/20 framing and foam, which maintains buoyancy while providing structural support to the faceplates and secure routes for pressure sensor cables. The width of the flap is 0.848 m, height 0.479 m, and thickness is 0.1365 m.

A cross-sectional view of the driveline is given in Fig 1.1b. Driveline design is motivated

by the goal of studying control schemes that go beyond approaches like linear damping. This requires precise control of torque and flap position throughout each period. A servo motor (Parker MPP092) and 15:1 gearbox (Parker PS90) permits both active and reactive control, and avoids additional losses introduced by belt-drives. Additionally, the motor-gearbox package allows for the driveline to be a self-contained unit below the flap. This reduces flow perturbations that would be caused by a larger form factor driveline. A rigid shaft coupling (R+W America BKC 150) connects the gearbox shaft and drive shaft which first passes through a 19-bit rotary encoder (Zettlex Midi Ultra IncOder) before being secured and sealed by a dual ball-bearing pack (Timken 6010 2RZ) and mechanical seal (Pac-seal Flowserve 21). Outside of the seal, the shaft interfaces with a roller plunger limit switch (Honeywell TTI 914CE2-6A) designed to disengage motor power at large angles of rotation as a safety measure. The drive shaft attaches to the flap through a six-axis load cell (ATI Mini 58). A second 6-axis load cell also connects the driven side of the flap to a freely-rotating shaft secured by another dual ball-bearing pack and mechanical seal. The driveline housing is secured to a base made up of steel plates and two large capacity vacuum pads (Anver VP1220A-NBR), which can be secured to any smooth surface. Vacuum pads are engaged by a dry-scroll vacuum pump (Agilent Technologies IDP3). The arrangement allows the OSWEC to potentially be deployed in a range of test facilities that allow two- and three-dimensional studies.

Data acquisition and control uses MATLAB Simulink. The software manages emergency stop systems, sends commands to a motor controller (Compax3 T10), and accepts data from OSWEC sensors using a National Instruments DAQ (PCI-6255). Following experiments, the

software saves data along with metainformation. Electrical isolation is maintained between all motor drive signals and the DAQ to reduce spurious noise.

1.3 Scope of Thesis

Operation of the laboratory-scale OSWEC will require precise control of flap angular position. However, the gearbox and shaft coupling may introduce non-linear differences in position between the motor and the flap. These nonlinearities could arise from gearbox backlash or coupling torsion, but the behavior is not adequately defined in manufacturer component specifications for the expected operational conditions. The scope of this thesis is to characterize positional differences resulting from the gearbox and coupling, and use findings to develop a correction to sinusoidal position control schemes. Other goals for this thesis include experimentally determining the motor torque and velocity constants, as future OSWEC experiments may require precise torque or velocity control and nominal values may not provide accurate characterizations. We note that non-linearity from the gearbox could be eliminated by a direct-drive configuration, but the required torque would necessitate a substantially larger motor frame size and heavier motor. As such, the amount of gearing included in this design is considered a potentially acceptable trade-off.

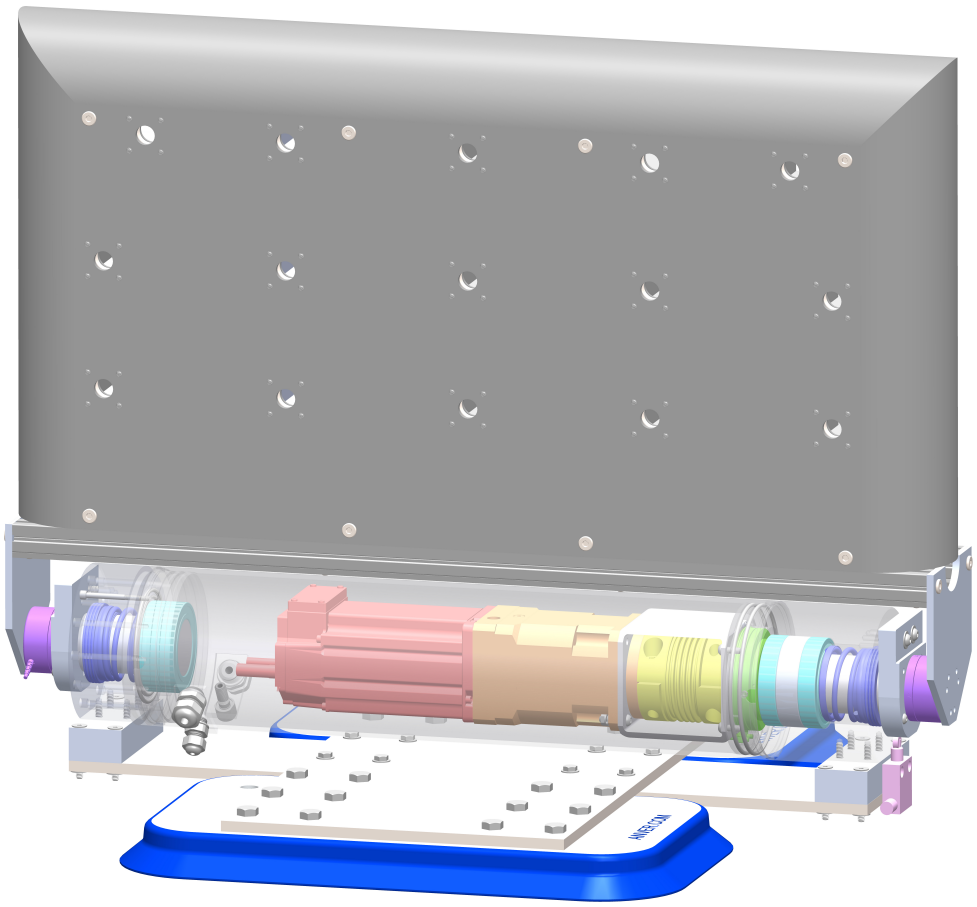

(a)

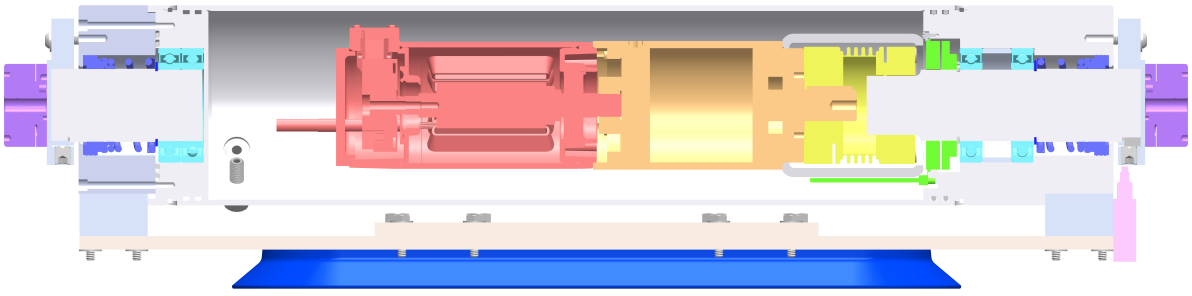

(b)

Figure 1.1: OSWEC design shown as a (a) full assembly and (b) section view of the driveline with the motor (red), gearbox (orange), coupling (yellow), encoder (green), bearings (light blue), seals (dark blue), limit switch (pink), and load cells (purple) highlighted.

Chapter 2

GEARBOX AND COUPLING COMPONENT TESTING

2.1 Methods

The gearbox and coupling may introduce differences between commanded and realized position. To study positional effects from the gearbox and coupling, we employed a benchtop dynamometer to emulate full system behavior (Fig. 2.1). The dynamometer is made up of 80/20 framing which supports the following components in-line: a servo motor, gearbox, rigid shaft coupling, encoder, six-axis load cell, bearing, flexible shaft coupling, and a magnetic particle brake. Components between the motor and load cell are the same as used in the OSWEC, while the bearing, flexible shaft coupling, and magnetic particle brake are specific to the dynamometer. Experiments were initially run without the bearing in the system. However, the rigid bellows coupling flexed under the weight of the driveline resulting in axial movement during operation. In addition to being an undesired degree-of-freedom, the axial movement also invalidated shaft encoder data as the spatial tolerance between rotor and shaft was not maintained. The flexible shaft coupling satisfies axial requirements of the magnetic particle brake, and shims were added to further reduce runout and rotary play. The magnetic particle brake (Placid industries PLB-100) was chosen due to its size and capacity (2-95 N-m), which encompasses the range of expected control torques during standard operation of the OSWEC.

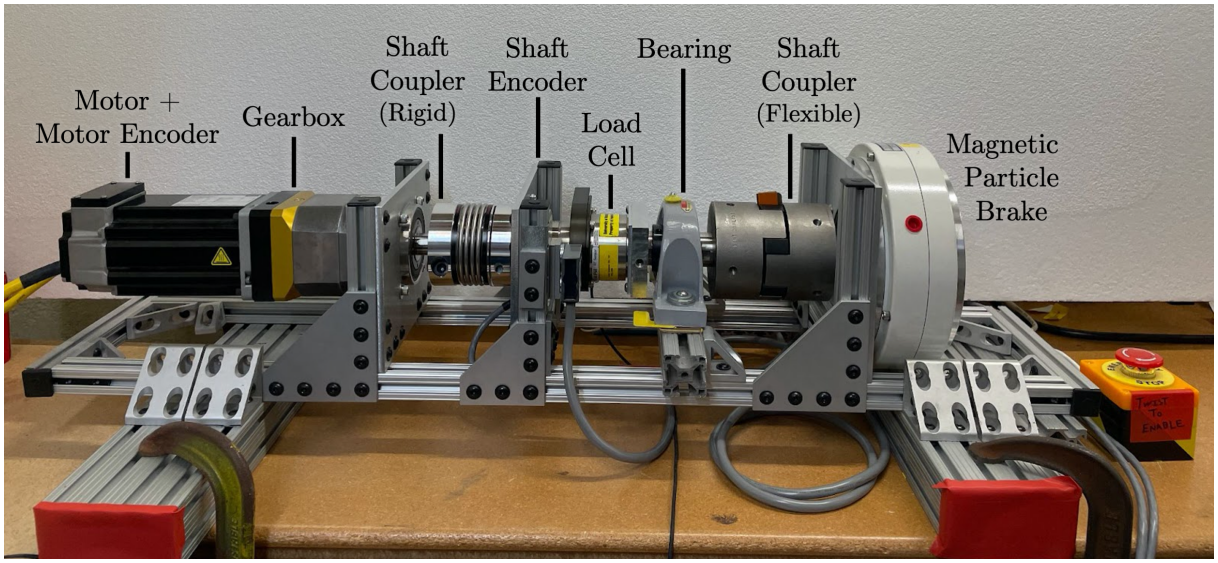

Figure 2.1: Mechanical components of the benchtop dynamometer.

In an inversion of OSWEC operation, the motor simulates hydrodynamic forcing from the flap as a result of interaction with a regular wave and the particle brake simulates motor resistance applied to the driveline in response. Because of this, the particle brake resistive torque (T_r) is specified as a constant linear damping scheme proportional to the rotational velocity ($\dot{\theta}_s$) measured by the shaft encoder as:

$$T_r = R\dot{\theta}_s, \tag{2.1}$$

where R is the damping coefficient. The load cell measures torque applied by the particle brake and parasitic torque from the bearing, though, bearing resistive torque is found to be minimal (Section 3.2.2). The motor encoder position (divided by the 15:1 gearbox ratio) is compared to the shaft encoder to characterize rotational offsets due to non-linearity.

Each experiment is defined by the amplitude and period of commanded oscillation, as

well as the resistive torque applied by the particle brake. Following ramp-up, an experiment contains 26 periods with each oscillation starting at the maximum amplitude position and following a cosinusoidal trajectory. The range of rotational amplitudes were chosen referencing experimental test results from prior research with a similar OSWEC [8]. The range of damping coefficients are based on the ideal power production values for an OSWEC in regular waves with 0.1 m wave height and 1, 1.5, and 2 s periods. This corresponds to the test conditions achievable in the Washington Air-Sea Interaction Research Facility (WASIRF), a wave flume at the University of Washington. Assuming the OWEC operates as a mass-spring-damper system with harmonic excitation and ideal damping, the ideal PTO damping coefficient is given as,

$$R_{PTO,opt} = \sqrt{\frac{[C - (I + \mu)\dot{\theta}^2]^2}{\dot{\theta}^2} + \nu^2}, \tag{2.2}$$

where C is the flap buoyancy (spring) constant, I is the second moment of inertia, μ is the coefficient of added mass, $\dot{\theta}$ is the rotational velocity, and ν is the coefficient of radiation damping [25]. All tests were conducted with a rotational period of 1.5 s, since varying the oscillation amplitude and damping coefficient emulates a range of shaft rotation rates and torque loads. Experimental conditions are summarized in Table 2.1. For all experiments, encoder and torque data were acquired at 1000 Hz.

As a consequence of the implementation of motor velocity control, absolute positional drift was exhibited throughout experiments. Since this drift is approximately linear, a Matlab function (detrend) is used to de-trend all position data prior to analysis. The magnitude of positional difference between the motor and shaft positions at each time step is defined as 'torsional deflection' and acts as a positional error metric. To evaluate trends in deflection,

phase shift and amplitude difference between the motor and shaft position measurements are calculated for each period of an experiment, as shown in Fig. 2.2.

Table 2.1: Experimental parameters. R is the particle brake damping coefficient. $|\theta|$ is the driveline oscillation amplitude.

	R [N-m-s]			
$\|\theta\|°$	42	62.5	83.3	104
5	x	x	x	x
10	x	x	x	x
15	x	x	x	x
20	x	x		x

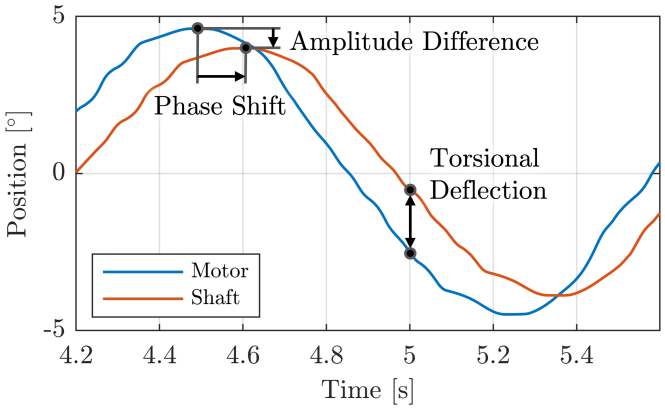

Figure 2.2: Parameters defined to evaluate positional error with positional differences exaggerated for clarity.

2.2 Results

An example of torsional deflection and driveline torque measured during each period is given in Fig. 2.3. The magnitude of deflection changes throughout a period, in response to changing driveline torque. However, cycle-to-cycle variation of deflection is negligible. While

deflection gives an instantaneous error measurement between the motor and shaft position, characterization of trends between experiments requires global metrics, such as phase shift and amplitude difference. Fig. 2.4 shows phase shift normalized as a percentage of period plotted against rms motor velocity, and Fig. 2.5 shows amplitude difference as a function of rms driveline torque. Phase shift is found to trend linearly with rms motor velocity ($R^2 = 0.81$), while amplitude difference trends linearly with rms driveline torque ($R^2 = 0.97$). The physical basis for the observed nonlinearity and a potential correction are now discussed.

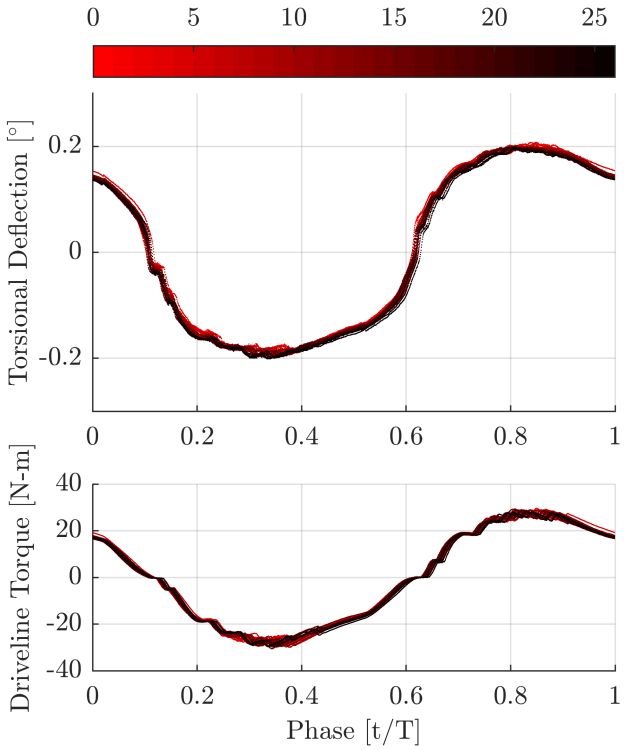

Figure 2.3: (Top) torsional deflection and (bottom) driveline torque with consecutive oscillations darkening in color with time for an experiment with $|\theta| = 15°$, and $R = 83.3$ [N-m-s].

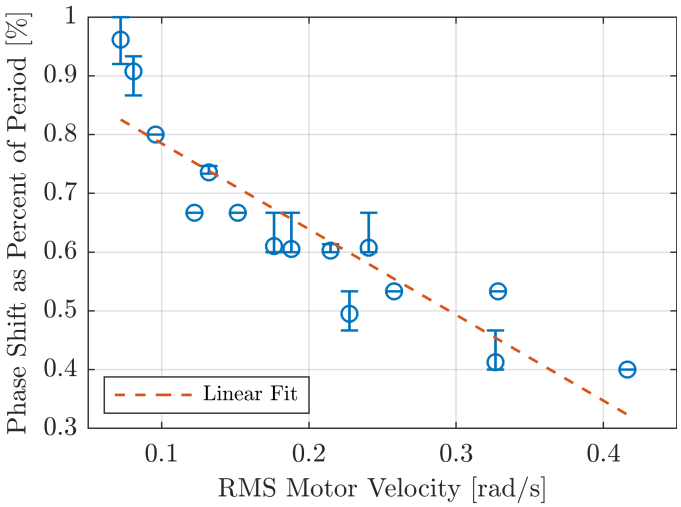

Figure 2.4: Phase shift statistics as a function of rms motor velocity.

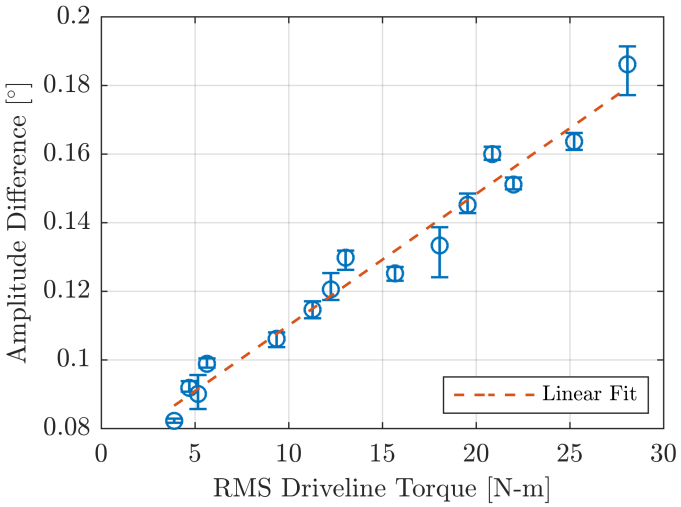

Figure 2.5: Amplitude difference statistics as a function of rms driveline torque.

2.3 Discussion

2.3.1 Sources of Phase and Amplitude Drifts

Phase shift between motor and shaft positions is a combined result of gearbox backlash and component torsion. Backlash introduces a phase shift by causing gear disengagement for a period of time following each direction change, and torsion causes a phase shift through its resulting offset in position. Phase shift from component torsion is estimated by assuming each material behaves as a linear torsional spring. Given this assumption, torque applied to the components (T) is related to the rotational displacement between motor and flap (γ) as,

$$T = k\gamma, \tag{2.3}$$

where k is the combined torsional stiffness constant of the coupling, shaft, and gearbox. Since components are connected in series, combined torsional stiffness is calculated as,

$$k = \frac{1}{\frac{1}{k_{coupling}} + \frac{1}{k_{shaft}} + \frac{1}{k_{gearbox}}} \tag{2.4}$$

[26]. Torsional stiffnesses of the gearbox and coupling are given in specifications as 41.25 kN-m/rad and 141 kN-m/rad respectively, while stiffness of the shaft is related to its modulus of rigidity ($G = 77.2$ GPa), diameter ($d = 0.042$ m), and length ($l = .089$ m) as,

$$k_{shaft} = \frac{G\pi d^4}{32l} \tag{2.5}$$

[27]. From this, phase shift resulting from component torsion is between 0.10 and 0.25 percent of the oscillation period for damping coefficients (R) of 42 and 104 N-m-s. This accounts for just over half of the phase shift experienced during high-velocity experiments, with the remaining shift attributable to dynamics other than component torsion (e.g. gearbox damping).

The trend of reduced phase shift with increasing rms motor velocity means that the faster the motor moves to a new position, the faster the driveline components respond - reducing the phase (temporal) lag between motor and flap connection point. Phase shift resulting from torsion of a linear spring is independent of oscillation velocity, so this trend is primarially due to gearbox backlash. As the rotation speed increases (i.e., greater amplitude oscillation, period held constant), the fraction of time within an oscillation that the gears spend disengaged is reduced. It follows that the magnitude of phase shift introduced by the gearbox is smaller during experiments with high velocity amplitude. Gearbox effects resulting from shaft acceleration could also contribute to this trend in phase shift, as velocity and acceleration vary dependently throughout experiments. Further experimentation with a range of oscillation periods is needed to determine the impact of gearbox effects resulting from shaft acceleration.

Amplitude differences between the motor and shaft positions are also a result of gearbox effects. During unloaded experiments (Section 3.2), an amplitude difference of approximately $0.025° \pm 0.015°$ is observed throughout experiments (Fig. 2.6). Since the driveline is unloaded, these amplitude differences are likely a result of backlash and coulomb damping (i.e., frictional losses). The trend of increasing amplitude difference with increasing driveline

torque is likely a result of increased coulomb damping, as it is proportional to the applied load [26].

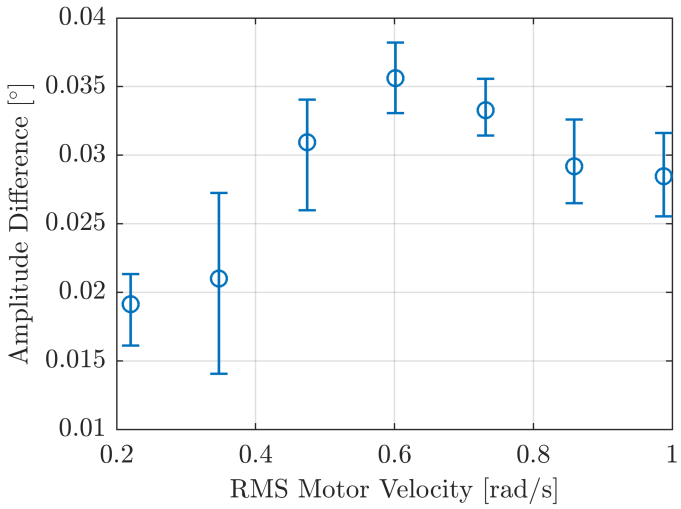

Figure 2.6: Amplitude difference statistics as a function of rms driveline velocity as measured by the motor, captured during unloaded experiments (Section 3.2).

2.3.2 Correction

A correction scheme for sinusoidal position control is developed from trends in phase shift and amplitude difference. In the absence of hardware available for testing, a proof-of-concept for this scheme is given by applying corrections to existing motor position data. First, position data is transformed to the frequency space using a fast Fourier transform (FFT), corrections are then applied in the frequency space as,

$$\Theta = (1 - \frac{\Delta|\theta|}{|\theta_m|})FFT(\theta_m)e^{-i\omega\varphi}, \tag{2.6}$$

where $\Delta|\theta|$ is amplitude difference, φ is phase shift, and ω is the frequency domain. Finally, the corrected motor position (Θ) is transformed back to the time domain using an inverse FFT.

The results of this proof-of-concept are given in Fig. 2.7, where the correction is applied to one period of existing motor position data, and Fig. 2.8, where mean, 5^{th}, and 95^{th} percentiles of torsional deflection are given for all experiments before and after the applied correction. While overall positional differences between the motor and flap are safely within $0.25°$, applying the correction should reduce this deflection to $< 0.12°$. This corresponds to the top of the flap being offset from the desired position by 1.3 mm if the correction is applied, and 3.0 mm otherwise. We expect that the baseline magnitude of positional error will be acceptable for planned studies, but the correction should be straightforward to implement and worthwhile.

In practical operation, this correction would be realized by amplifying the command amplitude and shifting oscillations in time given expected values of rms motor velocity and driveline torque. As driveline torque will not be a control parameter during OSWEC position control, experiments will need to be run without corrections, to capture torque for the given experimental conditions, prior to running experiments with a correction. Evaluation of the efficacy of this correction scheme requires further experimentation.

Finally, we note that an instantaneous correction could be implemented using the relationship between driveline torque and torsional deflection. Fig. 2.9 shows a piecewise linear relationship between phase-averaged instantaneous deflection and driveline torque. While an instantaneous scheme could improve position control of the flap, especially during higher

torques, it would be more difficult to implement and may not be necessary.

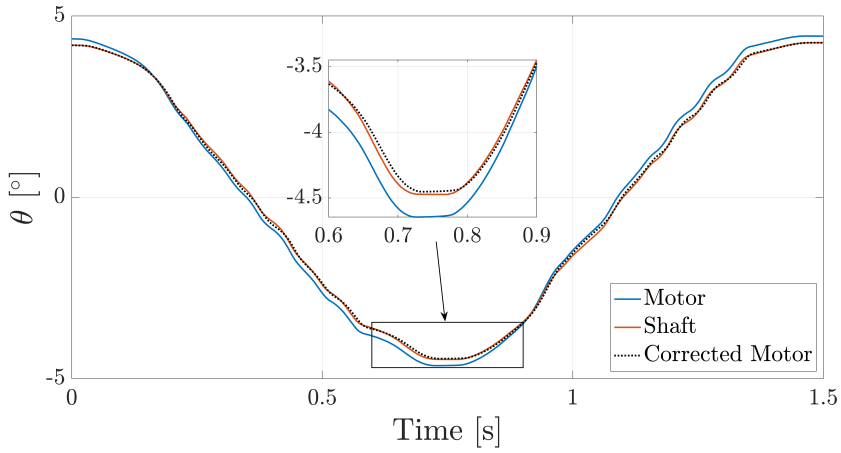

Figure 2.7: Motor, shaft, and corrected motor position during one period of an experiment with $R = 104$ N-m-s.

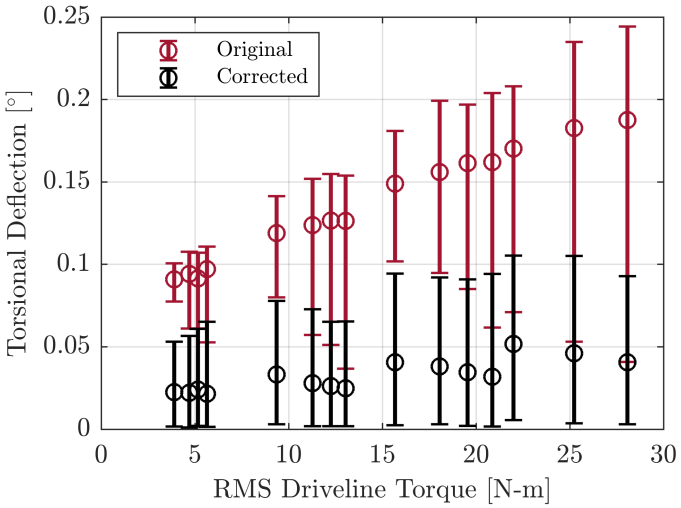

Figure 2.8: Torsional deflection of the shaft behind the motor before and after applying corrections to the motor position.

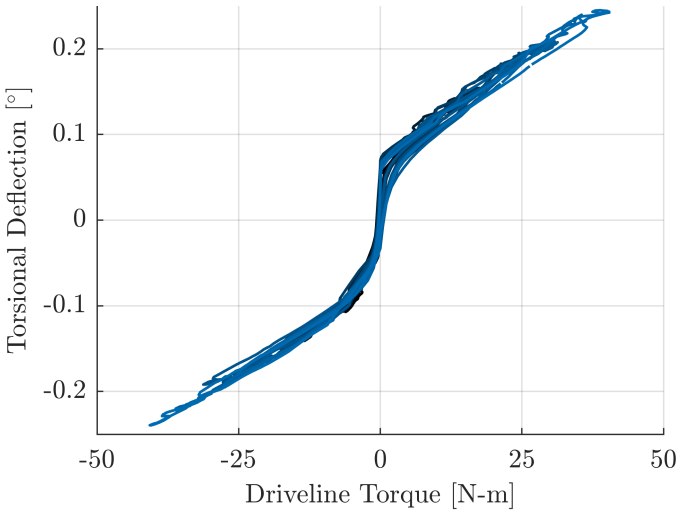

Figure 2.9: Phase-averaged torsional deflection as a function of driveline torque with a different shade of blue for each experiment.

Chapter 3
MOTOR CHARACTERIZATION

This section discusses characterization of the motor torque and velocity constants.

3.1 Motor Torque Constant

Future experiments will require OSWEC operation under torque control. During which, torque applied to the flap consists of mechanical torque applied by the gearbox, which should be a function of motor command current, less losses from the driveline seal. Characterization of the relationship between motor command current and driveline torque, along with characterization of seal losses will allow for more accurate torque control. Flap torque control can be achieved by measuring the torque from the load cells and using this as a control input. However, this must be interpreted by the MATLAB supervisory code and cannot be used directly by the motor drive. This limits the update rate for the command torque when signal smoothing is required.

3.1.1 Methods

Using the benchtop dynamometer (Fig. 2.1), a sinusoidal torque profile is commanded by the motor using torque control while the magnetic particle brake resists with its maximum torque of 95 N-m to prevent shaft rotation. Since OSWEC operation will require variable torques, a sinusoidal profile is selected as opposed to ramping up to constant values. This

allows the variability of torque constant to be evaluated given conditions expected during OSWEC testing. Driveline torque is measured using the six-axis load cell. All experiments have a torque oscillation period of 20 s, and run for a total time of 60 s (3 oscillation periods) following ramp-up. This longer period allows the gearbox more time to adjust to changing torques and minimizes the fraction of data captured during transitional periods between clockwise and counterclockwise torque, thus minimizing data artifacts from gearbox backlash. Table 3.1 gives current amplitudes and their nominal command torques ($T_{c,\ nom}$) for each experiment, where estimated motor command current (A) is calculated from the nominal values of maximum torque (11.54 N-m) and applied current (11.173 A) as,

$$A = (\frac{11.173\ \text{[A]}}{11.54\ \text{[N-m]}})(\frac{1}{15})T_{c,\ nom}. \tag{3.1}$$

Table 3.1: Motor torque control oscillation amplitudes.

[Amps]	T_c [N-m]
1.12	17.31
1.40	21.63
1.68	25.97
1.96	30.29
2.23	34.62
2.51	38.95
2.79	43.28
3.35	51.93
3.63	56.26
3.91	60.59
4.19	64.91
4.47	69.24

Here, torque constant is defined as the torque delivered by the gearbox relative to the motor command current. Clockwise and counterclockwise torque constants are calculated for each oscillation of an experiment by applying a linear fit to measured driveline torque as a function of command current (3.2), with the constant equal to the slope of the fit. The quality of fits are evaluated using R^2 values.

3.1.2 Results and Discussion

Fig. 3.1 shows commanded and realized driveline torque versus time for a given experiment. The relationship between command signal and torque output is linear while driveline torque is increasing. However, the response while commanded torque is decreasing indicates gearbox hysteresis. As the motor backs-off from peak torque, the realized driveline torque lags command until torque is increased again. This occurs in both directions and is suspected to be a result of gearbox stiction during stationary torque control. Conditions of a stationary driveline with alternating directions of control torque will not occur given a constant linear damping PTO scheme with control torque proportional to flap velocity. While a control scheme incorporating a spring-like term would result in high command torques during stationary instances, it would not result in any sustained periods of low-velocity with alternating control torque. Since conditions of a stationary driveline with alternating directions of control torque are not expected during OSWEC operation, torque constant values are calculated using selective data only during periods of torque ramp-up. These domains are shown in rectangles for a single experiment in Fig. 3.1.

Fig. 3.2 gives an example of clockwise and counterclockwise linear fits for one domain of

an oscillation. Torque constants are extracted from the linear fits from each oscillation of an experiment. From this, mean, minimum, and maximum torque constants are calculated (Fig. 3.3), along with R^2 values. The overall mean torque constant is 16.72 N-m/A, but values are spread between 15.56 and 18.42 N-m/A with clockwise values trending higher than counterclockwise. R^2 values indicate high-quality fits, with slightly improved fits during higher torque experiments.

Torque constant values are slightly higher for experiments with low rms driveline torque. This could be a result of variable gearbox efficiency, but more data would be needed to test this hypothesis. Accuracy could be improved slightly with the use of direction-dependent torque constants. However, with the spread of clockwise and counterclockwise values being 17% and 11% of their respective means, accurate torque control is not guaranteed without the implementation of real-time feedback from the load cell. Additionally, this direction dependency is not apparent in smaller previously-captured datasets, so further experimentation is needed for validation. Variation in torque constant could be a result of slight motion during experiments as the particle brake failed to completely restrict driveline movement, especially during torsional direction changes. Despite the data spread, the total average torque constant is in agreement with the manufacturer specification for the servomotor. After multiplying by the gear ratio (15), the specified torque constant is 16.845 N-m/A, which is within one percent of the mean value across all experiments.

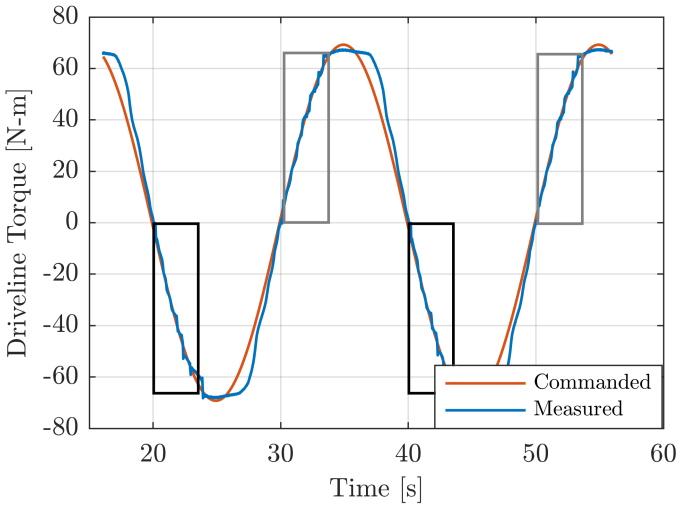

Figure 3.1: Commanded and measured driveline torque with time. Domains selected for computation of motor torque constant are given in black for clockwise and gray for counter-clockwise.

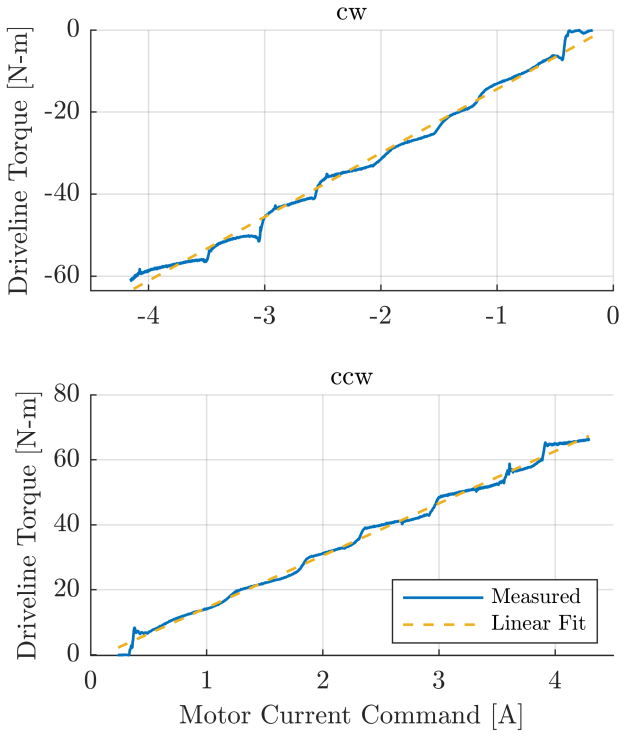

Figure 3.2: (Top) clockwise and (bottom) counterclockwise linear fits of driveline torque as a function of motor current command for the highest torque experiment.

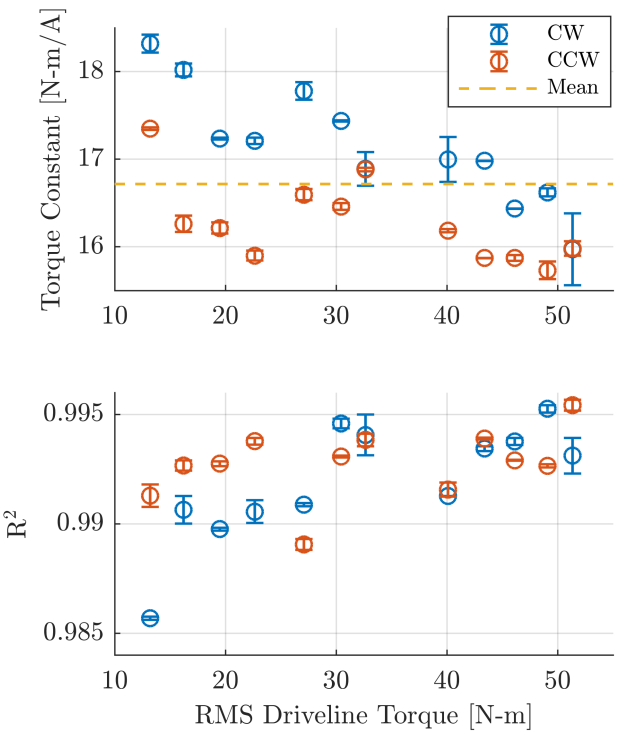

Figure 3.3: (Top) motor torque constant mean, min, and max values as a function of rms driveline torque above (bottom) mean, min, and max linear fit R^2 values.

3.2 Motor Velocity Constant

Accurate control of OSWEC position through motor velocity control requires a known relationship between shaft velocity and command voltage. While a nominal relationship could be used, an experimentally determined velocity constant should provide a more accurate representation of motor-gearbox response.

3.2.1 Methods

The benchtop dynamometer used in previous experiments is modified to exclude the flexible shaft coupling and magnetic particle brake, allowing the driveline to rotate freely (Fig. 3.4). Under velocity control, the motor commands a series of sinusoidal velocity profiles with

varying amplitudes while motor position data is captured by the motor's internal encoder, and driveline torque imposed by the bearing is measured with the six-axis load cell. To mimic OSWEC operation, all experiments have a period of 1.5 s and run for a total time of 60 s following ramp-up. A range of oscillation amplitudes is included in the experimental suite to provide redundancy (i.e., high velocity amplitude experiments contain all of the data points provided by experiments with lower velocity amplitudes), and to evaluate overall consistency of velocity constant throughout a range of conditions. The experimental suite, as given in Table 3.2, is designed to cover the full range of velocities expected during OSWEC operation. Estimated motor command voltage (V) is calculated from nominal values of maximum speed (37.5 rev/s) and voltage (10 V) as,

$$V = (\frac{10\ [\text{V}]}{37.5\ [\text{rev/s}]\ 2\pi})(\frac{1}{15})\dot{\theta}_{nom}. \tag{3.2}$$

Table 3.2: Motor velocity control oscillation amplitudes.

[Volts]	$\dot{\theta}_{nom}$ [rad/s]
0.23	0.37
0.35	0.55
0.47	0.73
0.58	0.92
0.70	1.10
0.81	1.28
0.93	1.46

Here, motor velocity constant is defined as the ratio between driveline rotational velocity, as measured by the motor's encoder, and motor command current. Motor velocity constant values are calculated in clockwise and counterclockwise directions for each oscillation of an experiment using a linear fit between rotational velocity and current command, with the quality of each fit indicated by an R^2 value. Linear positional drift is corrected using the MATLAB 'detrend' function prior to analysis and rotational velocity is calculated from motor encoder data using a moving window differentiator [28].

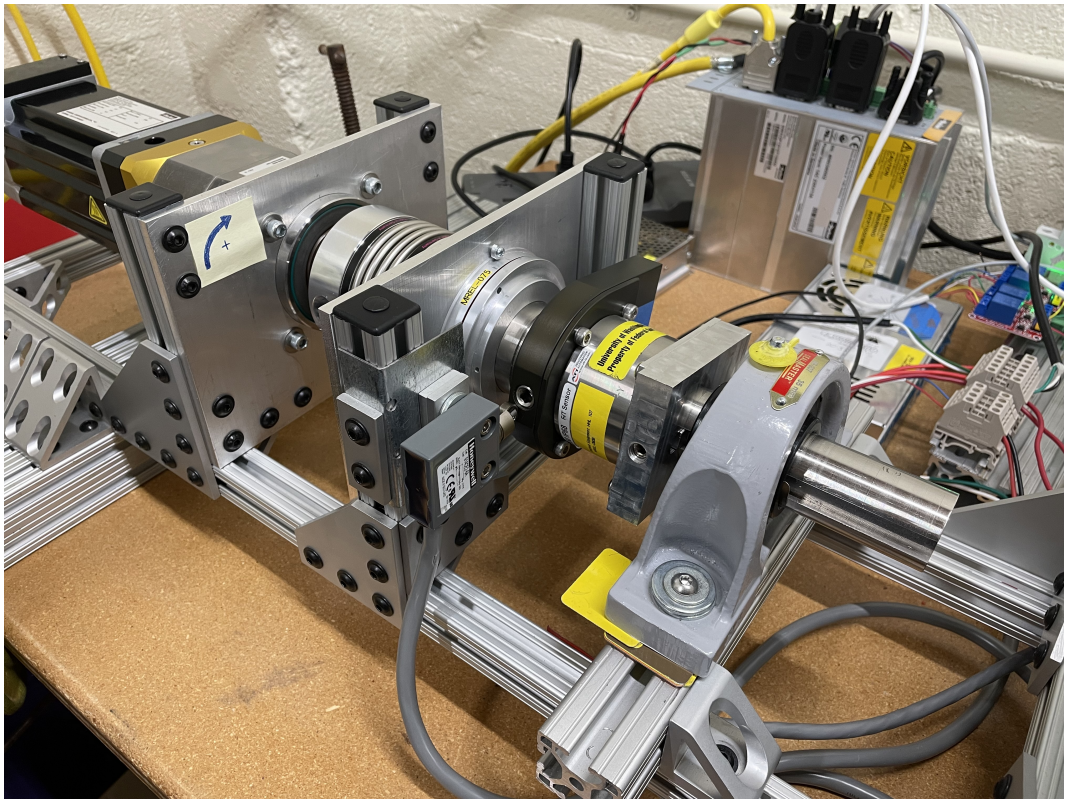

Figure 3.4: Mechanical components of the benchtop dynamometer modified to exclude the particle brake with the aim of operating with minimal driveline torque. The only source of torque in the system is the bearing, which is necessary to limit driveline runout.

3.2.2 Results and Discussion

The motor exhibits a delay at the start of rotations under velocity control, resulting in a lag throughout acceleration. It is able to operate as commanded during deceleration by undershooting the maximum velocity, but falls behind again once commanded to accelerate. The effect of this is proportionally greater during experiments with lower velocities, as apparent in Fig. 3.5 which gives the commanded and measured velocities during a portion of experiments with low and high velocity amplitudes. As shown in Fig. 3.7, this causes a larger spread in the estimated velocity constant for low-amplitude oscillations and lower R^2 values. Since experiments with lower-velocity amplitudes are redundant, as higher-velocity experiments also contain low-velocity data, calculating the velocity constant using only data from high-velocity experiments does not exclude any velocities expected during OSWEC testing.

We hypothesize that the delay may be a consequence of not tuning the motor controller for unloaded velocity control. The motor controller was tuned prior to dynamometer experiments but not re-tuned once the torsional load was removed from the driveline. This behavior is not apparent in any of the velocity-controlled experiments run under torsional load using the full dynamometer, and is not expected to be a problem for future OSWEC testing given the motor will be re-tuned and the flap will introduce inherent load to the driveline.

Assuming that the delay is unlikely in tests with a loaded driveline, the motor velocity constant is calculated using data from unaffected domains during deceleration, as shown within rectangles in Fig. 3.5. With the higher velocity experiments impacted by the delay proportionally less than lower velocity experiments, and the expectation that the delay is an

artifact of insufficient tuning to an unloaded driveline, it follows that motor velocity constant is more reliably aligned with the values calculated from large amplitude experiments.

Fig. 3.6 gives an example of the linear fit for clockwise and counterclockwise domains during an oscillation. Mean, minimum, and maximum velocity constants as calculated for each experiment along with fit R^2 values are given in Fig. 3.7. Velocity constants are similar in both directions and trend towards 1.5 rad/V-s with increasing rms motor velocity. The overall mean constant is 1.46 rad/V-s with values spread between 1.22 and 1.52 rad/V-s. Given the larger spread and fit error seen in low-velocity experiments (3.7, averaging data from only the three fastest experiments may give a more accurate result, as discussed prior. Mean velocity constants calculated as an average of data from top three and four fastest experiments are both 1.49 rad/V-s, with 2.8% spread relative to the mean of the top three experiments.

The bearing included in the driveline contributed slight torque to the system, with increased torque applied during higher velocity experiments as shown in Fig. 3.8. Total driveline torque as measured by the six-axis load cell remains under 0.4 N-m throughout all experiments, with the majority of values below 0.15 N-m. Bearing resistance appears to be asymmetric, with counterclockwise torque larger than clockwise. Since calculated velocity constants are independent of rotation direction, loading from the bearing during experiments does not appear to have impacted the results.

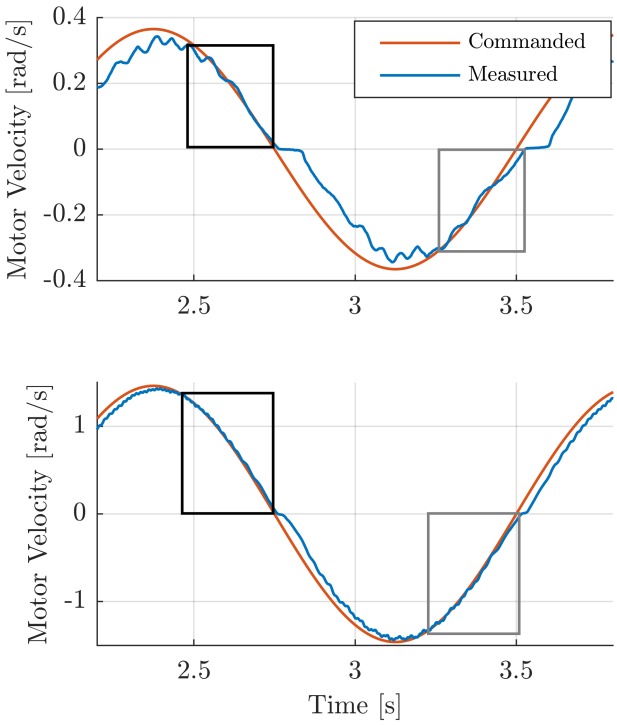

Figure 3.5: Commanded and measured motor velocity with time during a (top) low-velocity experiment, and (bottom) a high-velocity experiment. Domains selected for computation of motor velocity constant are given in black for clockwise and grey for counterclockwise.

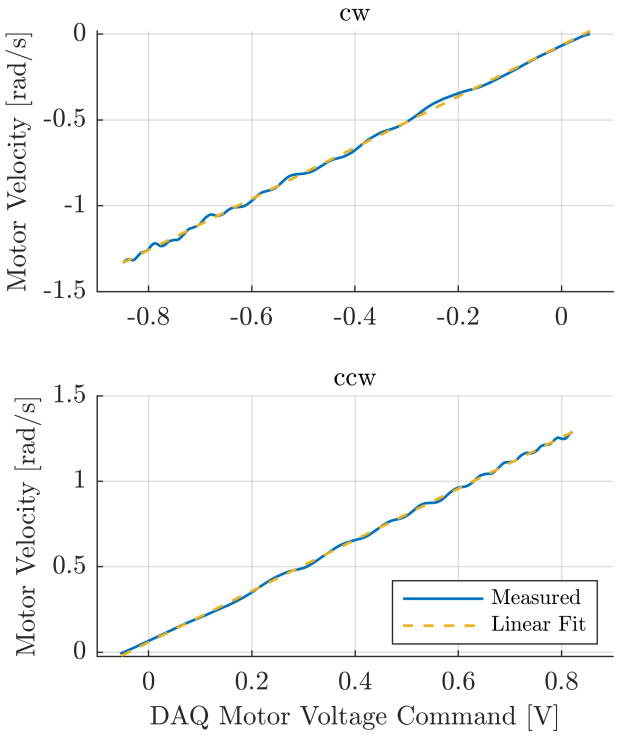

Figure 3.6: (Top) clockwise and (bottom) counterclockwise linear fits of driveline velocity as a function of motor current command for the highest velocity experiment.

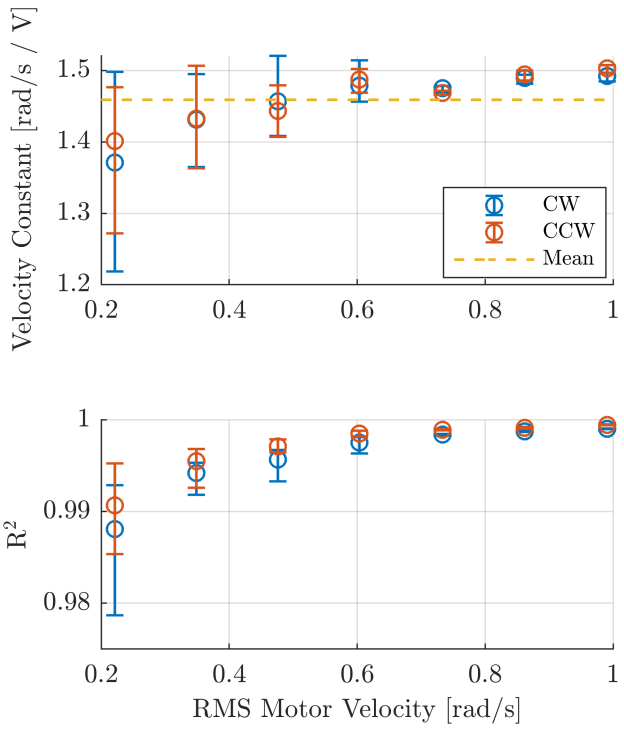

Figure 3.7: (Top) motor velocity constant mean, min, and max values as a function of rms motor velocity along with (bottom) mean, min, and max linear fit R^2 values.

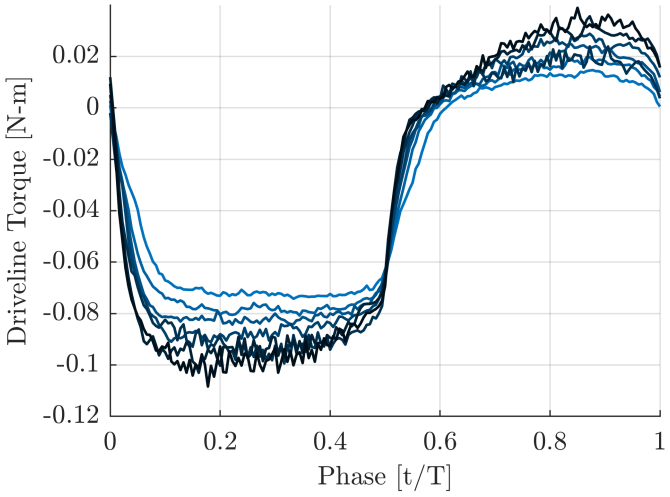

Figure 3.8: Phase-averaged driveline torque as a function of oscillation phase, with darker shades corresponding to higher-velocity experiments.

Chapter 4

CONCLUSION

This thesis summarizes the development and characterization of the driveline for a laboratory scale OSWEC. The OSWEC is designed to have PTO emulated by a servomotor and gearbox in-line with the pivot axis of the flap, protected by a waterproof housing and driveline seal. Using a motor to emulate PTO will allow a range of control schemes to be tested, in addition to supporting hydrodynamic characterization of the OSWEC. Some OSWEC experimentation will require precise control of flap position through motor velocity control, however, the gearbox and shaft coupling introduce differences between motor and drive shaft position which requires characterization. Additionally, velocity control requires an accurate relationship between command voltage and realized velocity, as quantified by a motor velocity constant. Other OSWEC experimentation will require precise control of driveline torque through motor torque control. This requires characterization of the relationship between motor torque and command current, in addition to characterization of the losses introduced by the mechanical seal of the driveline. To support these objectives, a benchtop dynamometer is designed and built to study positional differences under velocity control and to experimentally determine the motor torque and velocity constants.

The gearbox and rigid shaft coupling result in a measurable phase shift in time and amplitude attenuation between the motor and driveline positions. Relationships between

phase shift and motor velocity, in addition to amplitude attenuation and driveline torque, are used to develop a corrective scheme for sinusoidal velocity control which is found to reduce total torsional deflection between the motor and shaft to under 0.12°, a 50% reduction. Deflection could be reduced further with a stiffer coupling, but some deflection is inherent to the system as a result of the gearbox.

Motor characterization testing is performed using oscillatory torque and velocity control under conditions representative of OSWEC experiments. Average motor torque constant is found to be in agreement with manufacturer specifications, with under one percent error. However, the range of torque constant values calculated throughout the experimental suite is significant, so accurate torque control may require further testing or implementation of a corrective scheme. Average motor velocity constant has low variability once excluding data with motor tuning artifacts. Though oscillatory experiments resulted in additional work selecting domains for meaningful analysis, it also illuminated some of the motor control limitations. With variable torsional commands and a stationary driveline, realized torque lags commanded torque when the magnitude of command torque is decreasing. This is suspected to be a result of gearbox stiction, but further experiments would be required to explore this hypothesis. While these conditions are not expected for initial OSWEC experimentation, this lag may be meaningful for future control strategies. During velocity control of an unloaded driveline, a cut-in delay is observed. This delay is expected to be an artifact of poor motor tuning for an unloaded driveline and is not expected to impact OSWEC experiments in the future.

Further work is required to prepare the OSWEC for experimentation requiring torque

control. Because torsional losses and stiction are expected from the mechanical seal in the driveline, characterization of these losses is required to develop an accurate relationship between commanded torque and that realized by the flap. Seal loss characterization should be possible using the assembled OSWEC driveline and a similar analysis methodology as described in this thesis. Following torque characterization, initial experimentation using the OSWEC will focus on hydrodynamic characterization. This will be achieved by experimentally determining the flap center of mass, moment of inertia, and buoyant spring constant followed by the determination of excitation torque, added mass coefficient and damping coefficient. Finally wave response, with and without engaged PTO, will be evaluated through calculation of the response amplitude operator, a relation between device motion and incoming wave height. This hydrodynamic information will lay a foundation for interpreting future experiments with flap geometry and a range of control strategies.

BIBLIOGRAPHY

[1] United Nations. *Renewable energy - powering a safer future*. URL: https://www.un.org/en/climatechange/raising-ambition/renewable-energy (visited on 2022).

[2] Josh Humbert. *Ocean Power*. URL: https://drawdown.org/solutions/ocean-power (visited on 2022).

[3] M. Folley, T.J.T. Whittaker, and A. Henry. "The effect of water depth on the performance of a small surging wave energy converter". In: *Ocean Engineering* 34.8 (2007), pp. 1265–1274. DOI: 10.1016/j.oceaneng.2006.05.015.

[4] Alan Henry. "The Hydrodynamics of small seabed mounted bottom hinged wave energy converters in shallow water". Jan. 2009.

[5] Offshore Energy. *UK: Aquamarine Power Unveils Wave Energy Converter Oyster 800*. URL: https://www.offshore-energy.biz/uk-aquamarine-power-unveils-wave-energy-converter-oyster-800/ (visited on 2022).

[6] *The development of Oyster–A shallow water surging wave energy converter*. Proceedings of 7th European Wave Tidal Energy Conference. Jan. 2007.

[7] Yanji Wei, Ashkan Rafiee, Alan Henry, and Frederic Dias. "Wave interaction with an oscillating wave surge converter, Part I: Viscous effects". In: *Ocean Engineering* 104 (2015), pp. 185–203. ISSN: 0029-8018. DOI: 10.1016/j.oceaneng.2015.05.002.

[8] Dezhi Ning, C. Liu, Chongwei Zhang, M. Göteman, H. Zhao, and B. Teng. "Hydrodynamic performance of an oscillating wave surge converter in regular and irregular waves: An experimental study". In: *Journal of Marine Science and Technology (Taiwan)* 25 (Jan. 2017), pp. 520–530. DOI: 10.6119/JMST-017-0504-1.

[9] Moisés Brito, Rui M.L. Ferreira, Luis Teixeira, Maria G. Neves, and Ricardo B. Canelas. "Experimental investigation on the power capture of an oscillating wave surge converter in unidirectional waves". In: *Renewable Energy* 151 (2020), pp. 975–992. ISSN: 0960-1481. DOI: 10.1016/j.renene.2019.11.094.

[10] Alan Henry, Ashkan Rafiee, Pal Schmitt, Frédéric Dias, and Trevor Whittaker. "The Characteristics of Wave Impacts on an Oscillating Wave Surge Converter". In: 1 (May 2014), pp. 101–110.

[11] Yanji Wei, Thomas Abadie, Alan Henry, and Frederic Dias. "Wave interaction with an Oscillating Wave Surge Converter. Part II: Slamming". In: *Ocean Engineering* 113 (2016), pp. 319–334. ISSN: 0029-8018. DOI: 10.1016/j.oceaneng.2015.12.041.

[12] *A two dimensional experimental investigation of slamming of an Oscillating Wave Surge Converter*. Proceedings of the International Offshore and Polar Engineering Conference. Jan. 2014, pp. 296–305.

[13] *The Vertical Distribution and Evolution of Slam Pressure on an Oscillating Wave Surge Converter*. Proceedings of 34th International Conference on Ocean, Offshore, and Arctic Engineering. May 2015. DOI: 10.1115/OMAE2015-41290.

[14] *Extreme Loading on an Oscillating Wave Surge Converter*. Proceedings of 11th European Wave Tidal Energy Conference. Sept. 2015.

[15] Michael A. Choiniere, Nathan M. Tom, and Krish P. Thiagarajan. "Load shedding characteristics of an oscillating surge wave energy converter with variable geometry". In: *Ocean Engineering* 186 (2019), p. 105982. ISSN: 0029-8018. DOI: 10.1016/j.oceaneng.2019.04.063.

[16] Michael Choiniere, Jacob Davis, Nhu Nguyen, Nathan Tom, Matthew Fowler, and Krish Thiagarajan. "Hydrodynamics and load shedding behavior of a variable-geometry oscillating surge wave energy converter (OSWEC)". In: *Renewable Energy* 194 (2022), pp. 875–884. ISSN: 0960-1481. DOI: 10.1016/j.renene.2022.05.169.

[17] Moisés Brito, Rui Ferreira, Luis Teixeira, Maria Neves, and Luís Gil. "Experimental Investigation of the Flow Field in the Vicinity of an Oscillating Wave Surge Converter". In: *Journal of Marine Science and Engineering* 8 (Dec. 2020), p. 976. DOI: 10.3390/jmse8120976.

[18] Kelley Ruehl, Dominic D. Forbush, Yi-Hsiang Yu, and Nathan Tom. "Experimental and numerical comparisons of a dual-flap floating oscillating surge wave energy converter in regular waves". In: *Ocean Engineering* 196 (Nov. 2019). DOI: 10.1016/j.oceaneng.2019.106575.

[19] Pál Schmitt, Christian Windt, Jonathan Nicholson, and Björn Elsässer. "Development and validation of a procedure for numerical vibration analysis of an oscillating wave

surge converter". In: *European Journal of Mechanics - B/Fluids* 58 (2016), pp. 9–19. DOI: 10.1016/j.euromechflu.2016.02.005.

[20] *Hydrodynamic Loading on a Bottom Hinged Oscillating Wave Surge Converter*. Proceedings of the International Offshore and Polar Engineering Conference. Jan. 2012, pp. 550–557.

[21] *Design of an Oscillating Wave Surge Converter on the WindFloat* Structure*. Proceedings of 4th International Conference on Ocean Energy. Oct. 2012.

[22] Kelley Michelle Ruehl, Dominic Forbush, Pedro Lomonaco, Bret Bosma, Asher Simmons, Budi Gunawan, Giorgio Bacelli, and Carlos Michelen. "Experimental Testing of a Floating Oscillating Surge Wave Energy Converter". In: (Mar. 2019). DOI: 10.2172/1761877.

[23] L. Wilkinson, T.J.T. Whittaker, P.R. Thies, S. Day, and D. Ingram. "The power-capture of a nearshore, modular, flap-type wave energy converter in regular waves". In: *Ocean Engineering* 137 (2017), pp. 394–403. ISSN: 0029-8018. DOI: 10.1016/j.oceaneng.2017.04.016.

[24] *The Development of an Experimental Force Feedback Dynamometer to Investigate the Real Time Control of an Oscillating Wave Surge Converter*. Vol. Volume 8: Ocean Renewable Energy. International Conference on Offshore Mechanics and Arctic Engineering. June 2013. DOI: 10.1115/OMAE2013-10766.

[25] Johannes Falnes. *Ocean Waves and Oscillating Systems*. Cambridge University Press, 2004. ISBN: 0-521-78211-2.

[26] Derek Rowell and David N. Wormley. *System Dynamics: An Introduction*. Cambridge University Press, 2004. ISBN: 0-521-78211-2.

[27] Richard G. Budynas and Keith Nisbett. *Shigley's Mechanical Engineering Design, Ninth Edition*. McGraw-Hill, 2011. ISBN: 978-0-07-352928-8.

[28] Curtis J. Rusch, Ama R. Hartman, Benjamin D. Maurer, and Brian L. Polagye. "Influence of heave plate topology on reaction force". In: *Ocean Engineering* 241 (2021), p. 110054. ISSN: 0029-8018. DOI: 10.1016/j.oceaneng.2021.110054. URL: https://doi.org/10.1016/j.oceaneng.2021.110054.

[29] *Foundation Load Analysis of Oyster using a Five Degree of Freedom Load Transducer*. English. Proceedings of 8th European Wave Tidal Energy conference. 2009.

[30] *Determination of non-linear damping coefficients of bottom-hinged oscillating wave surge converters using numerical free decay tests*. 1st International Conference on Renewable Energies Offshore. Nov. 2014. DOI: 10.1201/b18973-71.

[31] Richard Manasseh, SA Sannasiraj, Kathleen L McInnes, V Sundar, and Purnima Jalihal. "Integration of wave energy and other marine renewable energy sources with the needs of coastal societies". In: *The International Journal of Ocean and Climate Systems* 8.1 (2017), pp. 19–36. DOI: 10.1177/1759313116683962.